ELSEVIER

Volume 184, Issue 11, November 2011

JOURNAL OF SOLID STATE CHEMISTRY

www.elsevier.com/locate/jssc

CONTENTS

Abstracted/indexed in BioEngineering Abstracts, Chemical Abstracts, Coal Abstracts, Current Contents/Physics, Chemical, & Earth Sciences, Engineering Index, Research Alert, SCISEARCH, Science Abstracts, and Science Citation Index. Also covered in the abstract and citation database SciVerse SCOPUS®. Full text available on SciVerse ScienceDirect®.

Regular Articles

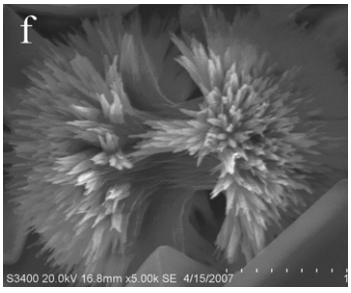

The well-defined aragonite hierarchical superstructures are formed using hexamethylenetetramine in aqueous solution.

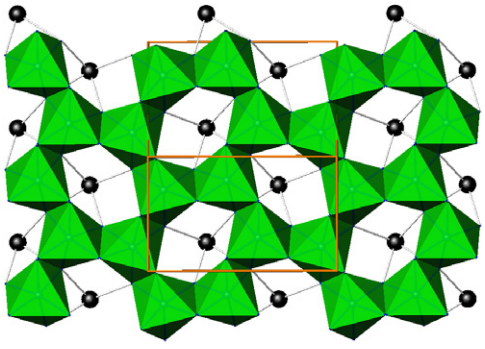

Actinide-bearing compounds with brannerite structure and their analog $CeTi_2O_6$ are not stable at high pressure. They were amorphized after ~20 GPa and a minor pressure-induced phase transition or decomposition process was always observed before amorphization.

Regular Articles—Continued

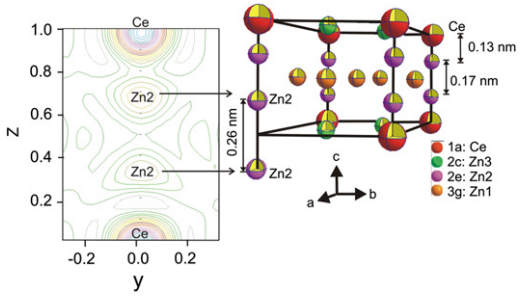

Existence of low temperature modification αCeZn$_7$ ($Ce_{1-x}Zn_{5+2x}$; x~0.33) of Ce_2Zn_{17} has been verified up to 750 °C that is attributed with the $TbCu_7$ type.

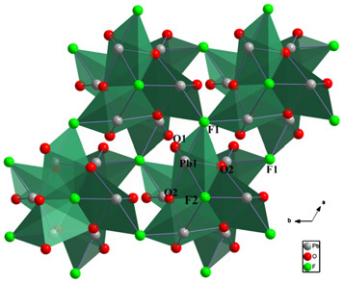

The Pb atoms are in the five coordination environments bonded to three O atoms and two F atoms to make up the distortional PbO_3F_2 polyhedra. Every six PbO_3F_2 polyhedra are connected by one F(1) atom to form the symmetrical structure, and then the distortion of the PbO_3F_2 polyhedra is offset.

Continued

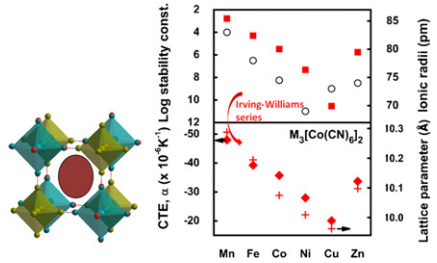

The structure of Prussian Blue analogs (PBAs) consists of two types of metal centered octahedral units connected by cyanide ligand. Lattice and interstitial water molecules are present in these framework structures. All the PBAs of the $M_3[Co(CN)_6]_2 \cdot nH_2O$ family show negative thermal expansion (NTE) behavior. The lattice parameters and magnitude of NTE correlates inversely with the Irving–Williams series of metal complex stability.

Conventional and microwave heating routes were used to prepare PET–LDH (polyethylene terephthalate–layered double hydroxide) composites with 1–10 wt% LDH by *in situ* polymerization. To enhance the compatibility between PET and the LDH, terephthalate or dodecyl sulphate was previously intercalated into the LDH. The microwave process improves the dispersion and the thermal stability of nanocomposites due to the interaction of the microwave radiation and the dipolar properties of EG and the homogeneous heating.

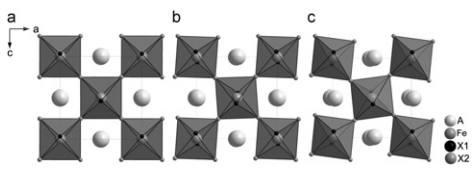

The crystal structures of the perovskites $La_{1-x}Sr_xFeO_{3-x}F_x$ for $x = 0.8$ (a), 0.5 (b) and 0.1 (c).

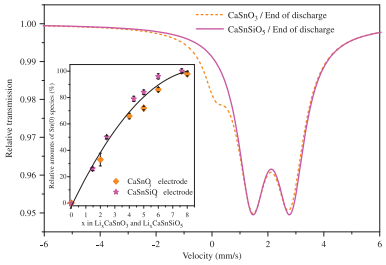

^{119}Sn Mössbauer spectra at the end of the first discharge of $CaSnO_3$ (dashed line) and $CaSnSiO_5$ (solid line) anodes for Li-ion batteries. Inset shows that relative amounts of Sn(0) based alloys formed during the first discharge are similar for $CaSnO_3$ and $CaSnSiO_5$ pristine materials.

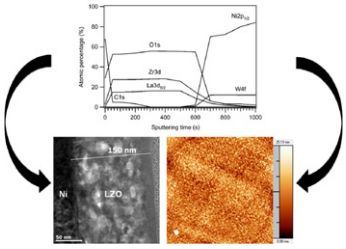

Thick LZO buffer layers from water-based precursor solutions were synthesized and their crystallinity, microstructure and buffer layer action were studied. The buffer layer action of the LZO layer was substantial to restrict the Ni penetration within 30 nm of a 140 nm thick film.

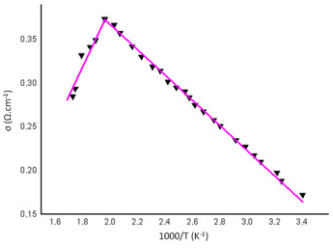

$DySr_5Ni_{2.4}Cu_{0.6}O_{12-\delta}$ exhibits a semi-conducting behaviour over the whole temperature range 294–579 K with a conductivity maximum of 0.4 S cm^{-1} at 510 K.

Synthetic approaches to borocarbonitrides, BC_xN ($x = 1–2$)
Nitesh Kumar, Kalyan Raidongia, Abhishek K. Mishra, Umesh V. Waghmare, A. Sundaresan and C.N.R. Rao
page 2902

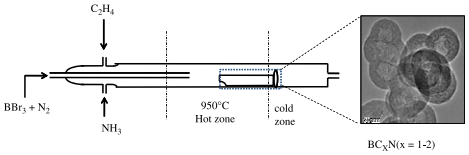

Vapor phase synthesis of BC_xN ($x = 1–2$) by the reaction of BBr_3, ethylene and ammonia leads to the formation of pan-like structure.

A general solution-chemistry route to the synthesis $LiMPO_4$ (M = Mn, Fe, and Co) nanocrystals with [010] orientation for lithium ion batteries
Jing Su, Bing-Qing Wei, Jie-Peng Rong, Wen-Yan Yin, Zhi-Xia Ye, Xian-Qing Tian, Ling Ren, Min-Hua Cao and Chang-Wen Hu
page 2909

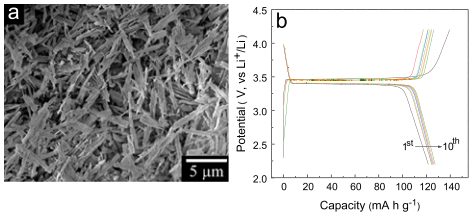

A general and efficient solvothermal strategy has been developed for the preparation of lithium transition metal phosphate micro-structures under solvothermal conditions in the presence of PVP.

Preparation of Pt deposited nanotubular TiO_2 as cathodes for enhanced photoelectrochemical hydrogen production using seawater electrolytes
Wonsik Nam, Seichang Oh, Hyunku Joo and Jaekyung Yoon
page 2920

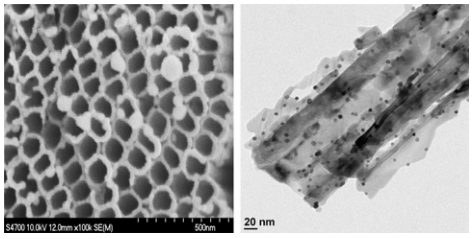

On the basis of photoelectrochemical hydrogen production, 0.2 wt% Pt/TiO_2 was observed to exhibit the best performance among the various Pt/TIO_2 cathodes with natural seawater. In comparison of hydrogen evolution rate with various seawater electrolytes, 0.2 wt% Pt/TiO_2 was found to show the better performance as cathode with the concentrated seawater electrolytes obtained from membrane.

High temperature crystal structures and superionic properties of $SrCl_2$, $SrBr_2$, $BaCl_2$ and $BaBr_2$
Stephen Hull, Stefan T. Norberg, Istaq Ahmed, Sten G. Eriksson and Chris E. Mohn
page 2925

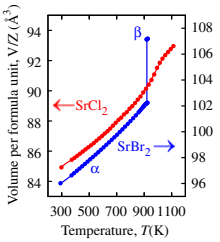

Anomalous behaviour of the lattice expansion of $SrCl_2$ at temperatures of ~1000 K is associated with the gradual transition to a superionic phase, whilst $SrBr_2$ undergoes a first-order structural transition ($\beta \rightarrow \alpha$) to a fluorite-structured superionic phase at 920(3) K.

TiO_2 nanorods branched on fast-synthesized large clearance TiO_2 nanotube arrays for dye-sensitized solar cells
Anzheng Hu, Haina Li, Zhiyong Jia and Zhengcai Xia
page 2936

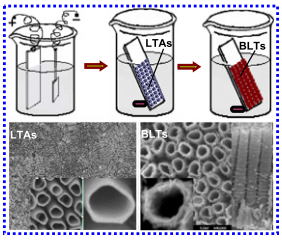

The schematic diagram of synthesis process for LTAs and BLTs is on the above and the corresponding FESEM images of obtained photoanodes samples are shown below.

Synthesis, structural characterization and magnetic properties of RE_2MgGe_2 (RE = rare-earth metal)
Nian-Tzu Suen, Paul H. Tobash and Svilen Bobev
page 2941

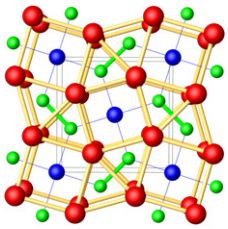

The structure of RE_2MgGe_2 (RE = Y, Nd, Sm, Gd–Tm, Lu) can be best viewed as 2-dimensional slabs of Mg and Ge atoms (anionic sub-lattice), and layers of rare-earth metal atoms (cationic sub-lattice) between them. Within this description, one should consider the Ge–Ge dumbbells (formally Ge_2^{6-}), interconnected with square-planar Mg atom as forming flat [$MgGe_2$] layers ($z = 0$), stacked along the c-axis with the layers at $z = 1/2$, made of rare-earth metal cations (formally RE^{3+}).

Continued

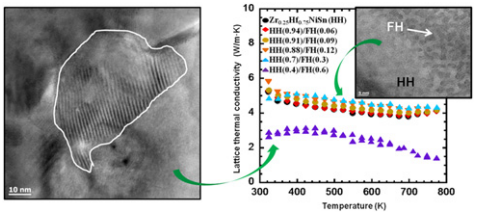

Large reduction in the lattice thermal conductivity of bulk nanostructured half-Heusler/full-Heusler ($Zr_{0.25}Hf_{075}NiSn$/$Zr_{0.25}Hf_{075}Ni_2Sn$) composites, obtained by solid-state diffusion at 1073 K of elemental Ni into vacant sites of the half-Heusler structure, arising from the formation of regions of spinodally decomposed HH and FH phases with a spatial composition modulation of ~2 nm.

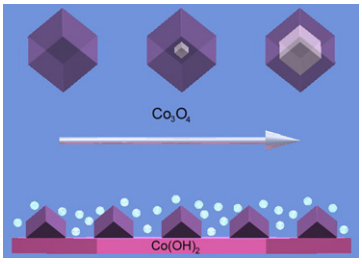

The formation mechanism of Co_3O_4 nanoboxes can be expressed as epitaxial growth of Co_3O_4 nanocubes from β-$Co(OH)_2$ nanoflakes due to a topotactic transformation and hollowing process owing to Ostwald ripening.

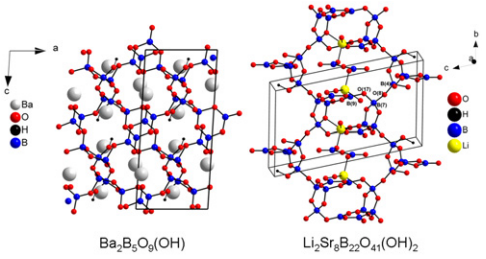

Novel hydrated borate structures.

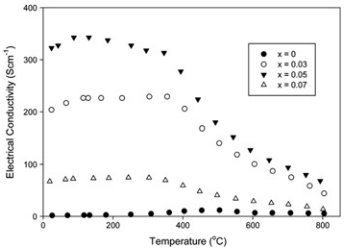

Phosphate/sulfate doping in $SrCoO_{3-y}$ leads to a structural change to a 3C-perovskite framework, with an accompanying large increase in conductivity.

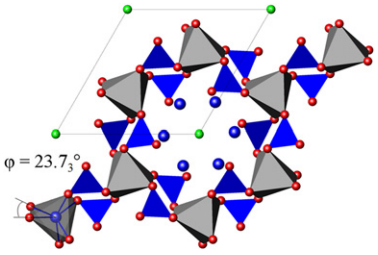

$[A^{I}]_4[A^{II}]_6(BO_4)_6X_2$ apatites can flexibly accommodate numerous cationic, metalloid and anionic substitutions. Using a combination of new refinements and published structures, this paper reviews correlations between substituent type and framework adaptation through adjustment of the $A^{I}O_6$ metaprism twist angle, φ.

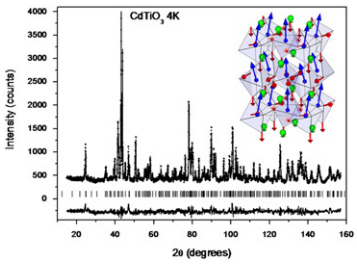

The structure of three phases of $CdTiO_3$ have been refined using high resolution powder neutron diffraction data. This involved the preparation of samples enriched in ^{114}Cd. Cooling perovskite-type $CdTiO_3$ to 4 K results in a ferroelectric phase in $Pna2_1$.

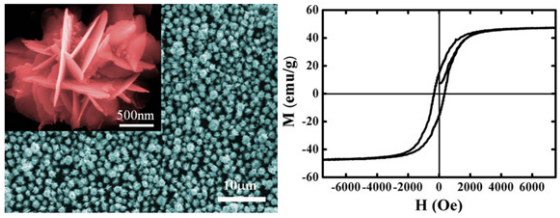

Monodispersed Ni flower-like architectures composed of nano-flakes were synthesized through a facile solvent-thermal process. The Ni architectures exhibited a large coercivity and enhanced electromagnetic wave absorption in GHz.

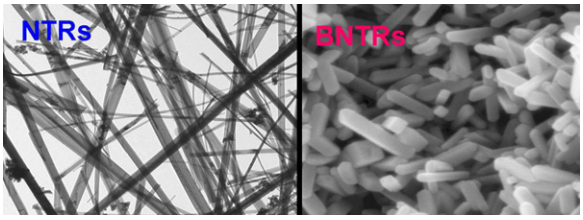

Boron and nitrogen codoped TiO_2 nanorods (BNTRs) were synthesized using TiN. The BNTRs showed a higher photocatalytic activity and a bigger photocurrent than N–TiO_2 nanorods (NTRs) under visible light irradiation.

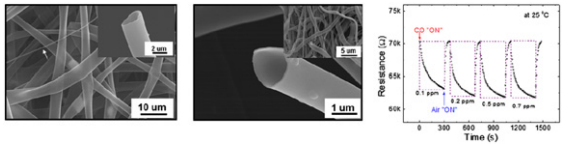

Microstructures of as-prepared and calcined hollow TiO_2 fibers prepared by the electrospinning technique with a coaxial needle. Dynamic response at various CO concentrations for the sensor fabricated with the hollow TiO_2 fibers.

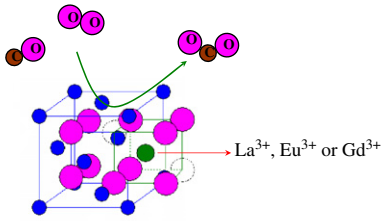

In this work, $Ce_{0.9}M_{0.1}O_{2-\delta}$ mixed oxides (M = La, Eu and Gd) were synthesized by coprecipitation. Independent of the dopant cation, the obtained solids maintain the F-type crystalline structure, characteristic of CeO_2 (fluorite structure) without phase segregation. The ceria lattice expands depending on the ionic radii of the dopant cation, as indicated by X-ray diffraction studies. This effect also agrees with the observed shift of the F_{2g} Raman vibrational mode. The presence of the dopant cations in the ceria lattice increases the concentration of structural oxygen vacancies and the reducibility of the redox pair Ce^{4+}/Ce^{3+}. All synthesized materials show higher catalytic activity for the CO oxidation reaction than that of bare CeO_2, being Eu-doped solid the one with the best catalytic performances despite of its lower surface area.

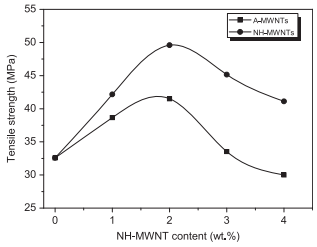

This describes the increase of mechanical properties in NH-MWNTs–g-PMMA hybrid composites with different NH-MWNT contents.

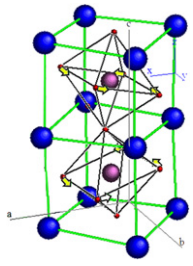

Raman active mode in LuAP crystal.

Continued

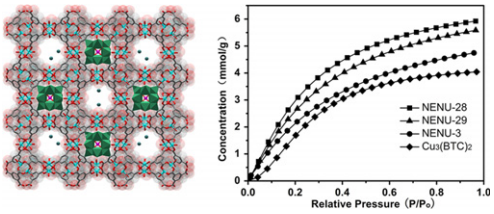

The adsorption behavior of volatile organic compounds in porous metal–organic frameworks functionalized by polyoxometalates has been systematically evaluated.

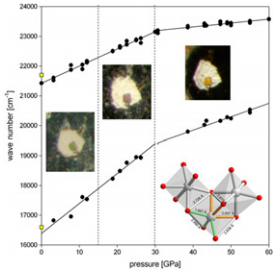

New synchrotron single-crystal x-ray diffraction experiments to 55 GPa in Ne and He complemented by measurements of optical absorption spectra show no indication of the earlier reported monoclinic distortion at 15–30 GPa, but indicate evidence of two discontinuous transitions of electronic or magnetic nature, most likely associated with a change in the magnetic ordering and charge transfer. The compression mechanism established from single crystal refinements indicates much smaller distortion of the Cr^{3+} coordination environment than was previously assumed.

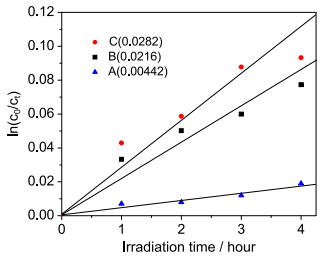

High visible active nano-sized $BiVO_4$ photocatalyst with large surface area is successfully synthesized, which is attributed to the chelating role of EDTA group inhibiting the growth of $BiVO_4$ crystallites.

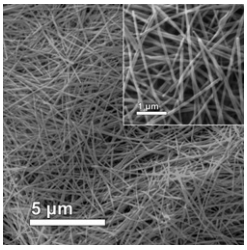

Cobalt sodium tartrate nanowires with smooth surfaces are synthesized hydrothermally. Their narrowly distributed diameters decrease with reaction time after initial two hours and are controllable from 80 to 250 nm.

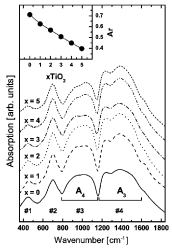

Behavior of the relative integrated intensity of the IR bands, $Ar = A_4/A_3$, as TiO_2 content increases. A decrease of 45% of Ar indicates that the number of BO_4 groups is decreasing due to the $BO_4 \rightarrow BO_3$ back conversion.

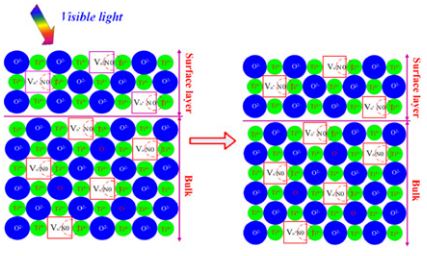

Synergistic action is realized between $(V_o^{\bullet})_{bulk}$ and $(V_o^{\bullet\bullet})_{surf}$ in the presence of active structures $(V_o^{\bullet})_{bulk}$–NO–Ti and $(V_o^{\bullet\bullet})_{surf}$–NO–Ti.

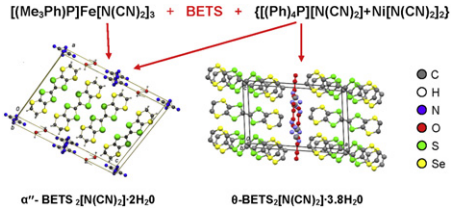

We studied electrochemical oxidation of BETS donor in the presence of simple and/or complex dicyanamides of transition metals (Ni, Fe, Mn) as electrolytes. New conducting salts α″-$BETS_2[N(CN)_2]\cdot 2H_2O$ and θ-$BETS_2[N(CN)_2]\cdot 3.8H_2O$ have been synthesized and characterized.

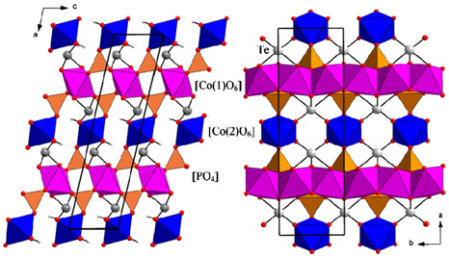

The new compound $Co_3Te_2O_2(PO_4)_2(OH)_4$ has been synthesized using hydrothermal techniques. It crystallizes in the monoclinic space group $C2/m$. Building blocks are $[Co(1)O_6]$, $[TeO_3(OH)_2]$, $[PO_4]$ and $[Co(2)O_2(OH)_4]$. The magnetic susceptibility shows two antiferromagnetic transitions at 21 K and 4 K, respectively.

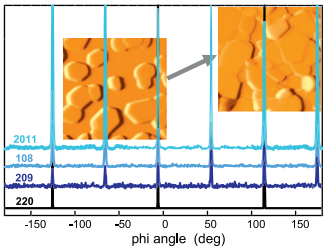

XRD and AFM patterns of $SrFe_{12}O_{19}$ thin film epitaxially grown on $SrTiO_3(111)$ single crystal using seeding layer templating.

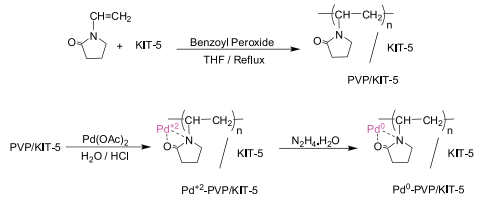

Pd-poly(N-vinyl-2-pyrrolidone)/KIT-5 was prepared as an organic–inorganic hybrid catalyst for the Suzuki–Miyaura reaction. The stability of the catalyst was excellent and could be reused 8 times in the Suzuki–Miyaura reaction.

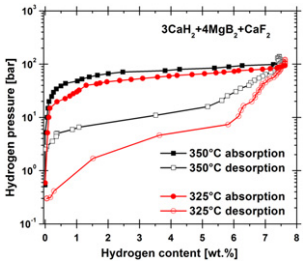

PCI of $3CaH_2 + 4MgB_2 + CaF_2$ reactive hydride composite at 325 °C and 350 °C. Open marks: dehydrogenation, closed marks: hydrogenation.

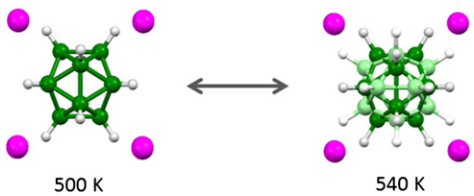

$Cs_2B_{12}H_{12}$ undergoes an order–disorder phase transition near 529 K. Similar transitions are observed for $K_2B_{12}H_{12}$ and $Rb_2B_{12}H_{12}$.

Continued

Synthesis, structure and physical properties of reduced barium titanate $Ba_2Ti_{13}O_{22}$

Kunimitsu Kataoka, Norihito Kijima, Hiroshi Hayakawa, Akira Iyo, Ken-ichi Ohshima and Junji Akimoto

page 3117

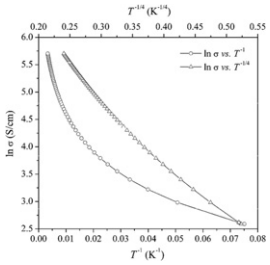

Temperature dependence of the electrical conductivity of $Ba_2Ti_{13}O_{22}$. A plot of $\ln \sigma$ versus T^{-1} is shown by open circles, and a plot of $\ln \sigma$ versus $T^{-1/4}$ is shown by open triangles.

Two multi-dimensional frameworks constructed from zinc coordination polymers with pyridine carboxylic acids

Yuanyuan Guo, Pengtao Ma, Jingping Wang and Jingyang Niu

page 3121

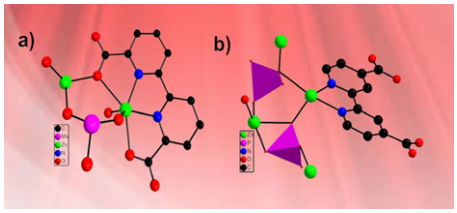

Two new transition metal coordination polymers, namely, $[Zn_2(H_2O)L_1(MoO_4)]_n$ (**1**), $[Zn_4(PO_4)_2L_2(H_2O)]_n$ (**2**) (H_2L_1 = 2,2′-bipyridine-6,6′-dicarboxylic acid, H_2L_2 = 2,2′-bipyridine-4,4′-dicarboxylic acid) have been hydrothermally synthesized. **1** represents a 2-D sheet structure while **2** represents 3-D network.

Low-temperature structural phase transition in synthetic libethenite Cu_2PO_4OH

Alexei A. Belik, Panče Naumov, Jungeun Kim and Shunsuke Tsuda

page 3128

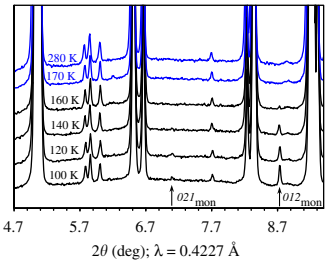

Fragments of experimental synchrotron X-ray powder diffraction patterns of Cu_2PO_4OH between 100 and 280 K. Arrows show additional reflections that appear below 160 K in the monoclinic $P2_1/n$ phase.